J. Fluid Mech. (1979), *vol.* 93, *part* 1, *pp.* 135–159
Printed in Great Britain

Instability and turbulence in a stratified fluid with shear

By C. G. KOOP† AND F. K. BROWAND
Department of Aerospace Engineering, University of Southern California, Los Angeles, California 90007

(Received 6 February 1978 and in revised form 8 September 1978)

1. Introduction

The experimental measurements presented here describe the major features of the turbulence produced by shearing instability in a miscible, two-fluid system with a statically stable density difference. The parameter range is such that buoyancy forces have an important dynamical effect on the turbulence. The motivation for this study is the accumulating body of oceanic field measurements which suggest the importance of shear-induced turbulent mixing in the oceans of the world, particularly in coastal environments or where waters of different origin meet. The oceanic situation is, of course, more complicated than the laboratory simulation. The density stratification in the ocean is often produced by two diffusive constituents and the difference in these rates of molecular diffusion can be a source of energy for double-diffusive instabilities. There is usually horizontal shear present, and the shear may be all, or in part, time dependent on the scale of the turbulent event itself. These complications have been neglected, and one may regard the present experiment as applicable in the limit of steady shear applied on a time scale longer than the turbulent event, and of a magnitude large enough to ignore any possible double-diffusive process. Two major ingredients are present; the shear flow, which supplies turbulent energy, and stable stratification which, in general, has an inhibiting effect upon the turbulence.

2. Experimental apparatus and procedure

2.1. *Apparatus*

The experiment was performed in a water channel shown schematically in figure 1. Briefly, two parallel streams of water having different densities (salinities) and moving at different velocities are merged at the entrance to the channel. The resulting instability and turbulence evolves spatially as the fluid is convected downstream. The test section is 10 by 10 by 160 cm and has a free surface to allow for the introduction of probes at any longitudinal location. Flow velocities within the channel may be varied between 1 and 15 cm/s and the freestream turbulence level is about 0·5 %. Dye may be introduced into the boundary layer on the upper side of the splitter plate, thus marking the interface between the two streams. In addition, the density field may be visualized using the shadograph technique.

Figure 2 shows the geometry of the flowfield at the entrance to the test section. The initial shear region is characterized by an overall velocity difference ΔU and density

† Fluid Mechanics Department, TRW Defense and Space Systems Group, Redondo Beach, California 90278.

0022–1120/79/4224–6660 $02.00

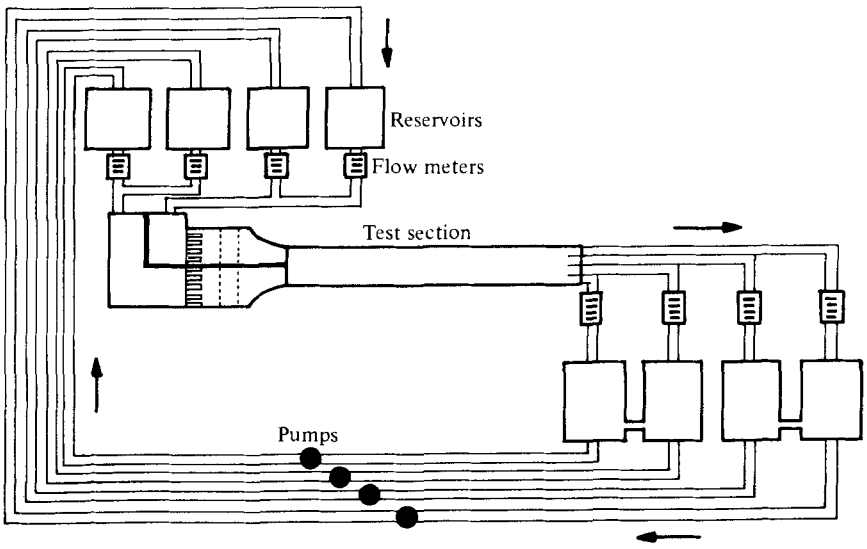

FIGURE 1. Sketch of the experimental apparatus.

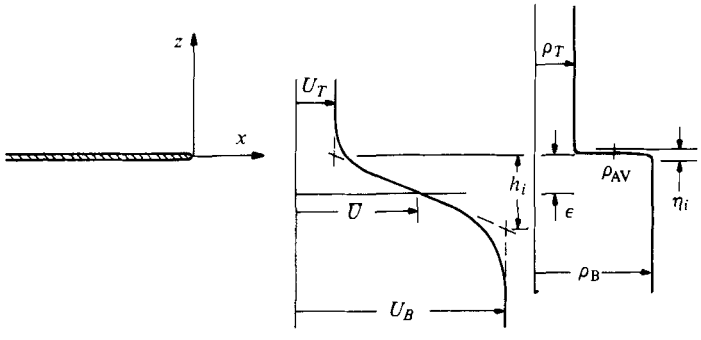

FIGURE 2. Initial shear layer geometry: initial Richardson number, $0{\cdot}05 \leqslant Ri \leqslant 0{\cdot}2$; initial Reynolds number, $Re \approx 300$; maximum Reynolds number, $300 < Re_{MAX} < 1900$; $h_i/\eta_i \gg 1$.

difference $\Delta\rho$. The shear layer has an initial vertical length scale (maximum slope thickness) h_i and the corresponding density scale is denoted as η_i. The mean convection speed of the fluid in the channel is $\overline{U}$, the average density is ρ_{AV}, and the gravity, g, acts vertically downward. Note that the centre of the shear region is displaced vertically by a small amount, ϵ, from the density interface.

Consistent with the Boussinesq approximation, the density difference appears only in connexion with the gravity field as $g\Delta\rho/\rho_{AV}$. Including the kinematic viscosity, ν, and the diffusion coefficient for salt D, the flowfield is uniquely determined by the six non-dimensional quantities

$$Ri = g\Delta\rho h_i/\rho_{AV}(\Delta U)^2; \quad Re = \Delta U h_i/\nu;$$
$$Sc = \nu/D; \quad \Delta U/\overline{U}; \quad \epsilon/h_i; \quad \eta_i/h_i.$$

Ri and Re are the initial Richardson number and Reynolds number and measure respectively the importance of buoyancy and viscosity upon the developing instability. h_i is the maximum slope thickness of the shear layer at $x = 1$ cm. The value of

Ri	Re	$\frac{\Delta\rho}{\rho_{AV}}$
0·05	300	0·0085
0·075	300	0·0128
0·1	300	0·017
0·125	300	0·0213
0·15	300	0·0255
0·2	300	0·034
0·075	200	0·0037
0·075	250	0·0084
0·075	300	0·0128
0·075	350	0·0238

TABLE 1. Summary of test conditions. For all the above cases $\Delta U/\bar{U} = 1{\cdot}10$.

h_i determines the scale of the initial instability which visually appears at about $x = 3$ cm. Within the first few centimetres h_i is almost constant (it grows less than 15 % between the splitter plate and $d = 5$ cm). The quantities η_i/h_i and ϵ/h_i introduce additional degrees of freedom not discussed in previous experiments by Thorpe (1973*a*, *b*) or Delisi & Corcos (1973) who considered the case $\eta_i/h_i \approx 1, \epsilon/h_i \approx 0$. In the present work, however, $\eta_i/h_i \ll 1, \epsilon/h_i \approx \frac{1}{2}$ and it will be shown that several important features of the turbulent mixing arise from this initial disparity in length scales.

The Richardson number as defined above is a global measure of the importance of buoyancy. The distribution of *gradient* Richardson number, $g(d\rho/dz)/\rho(dU/dz)^2$, through the sheared region would progress from zero values at the outer edges to a local maximum somewhere within. (The product $R_i h_i/\eta_i$ would be the local maximum value of the gradient Richardson number for $\epsilon = 0$.) For most of the experiments, the Richardson number alone was varied over the range $0{\cdot}05 \leqslant Ri \leqslant 0{\cdot}2$. Four cases were run at a fixed Ri but at different values of Re to test the sensitivity of the results to variations in Reynolds number. Table 1 summarizes the test conditions. A discussion of the practical constraints which influence the choice of these test conditions is given in Koop (1976).

2.2. *Procedure*

Quantitative measurements of the flowfield were made at 12–15 longitudinal locations by slowly traversing the mixing region in the vertical (z) direction with a hot-film anemometer and a conductivity probe (separated laterally by 1 cm). The hot-film probe used was a TSI 0·05 mm cylindrical sensor operated at constant temperature in the anemometer circuit described by Weidman & Browand (1975). The conductivity probe, similar to those discussed by Maxworthy & Browand (1975), was operated in an a.c. bridge at 50 kHz, and had a measured resolution of about 0·3 mm. In addition to this sensor, a second, smaller conductivity probe subsequently referred to as the microprobe, was used in one phase of the experiment for measuring the small-scale structure of the turbulence. Its resolution was measured to be better than 0·05 mm. The vertical descent rate varied between 0·003 and 0·01 cm/s, so that about 1800 large-scale structures were sampled in the 15–30 min required to cross the mixing region. Data were recorded on FM tape, and later digitized at 50 Hz. The microprobe data were digitized at 300 Hz.

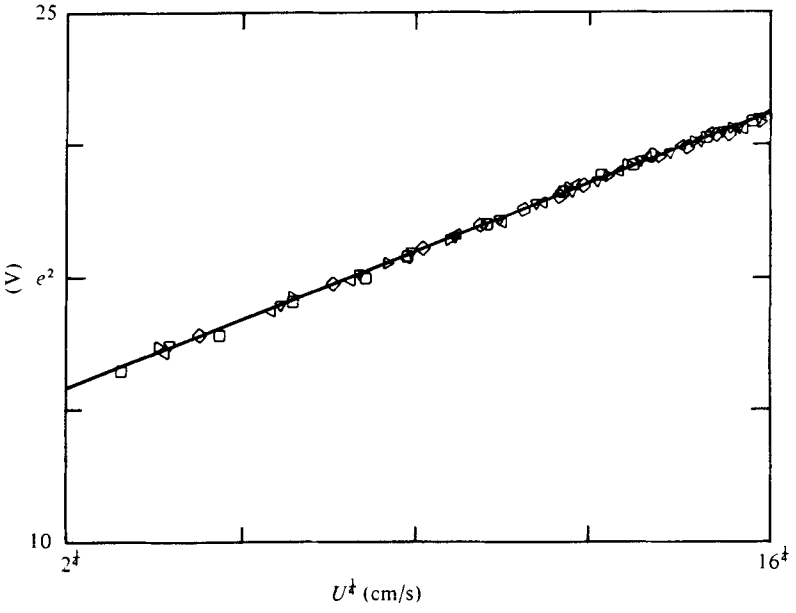

FIGURE 3. Typical hot-film calibration.

Constant salinity baths were used to calibrate the conductivity probe before every run. In addition, the supply tank densities were continually monitored with sensitive hydrometers so the layer densities above and below the mixing region were accurately known. The hot film sensor was calibrated before and after each run, by allowing the instrument carriage, supported on an air bearing, to accelerate to terminal speed along the slightly inclined track. The hot film travelled through quiescent water and the velocity of the carriage was determined by differentiating the carriage position signal. This free fall operation was necessary to avoid unwanted probe vibration. A typical calibration result is shown in figure 3. The average variance of the data is about 0·15 cm/s, which is roughly 1–2 % of ΔU.

Mean profiles of velocity and density are computed in the data reduction program by evaluating

$$\bar{u}(z) = (1/N)\sum_{j=1}^{N} u_j,$$

$$\bar{\rho}(z) = (1/N)\Sigma\rho_j,$$

and

$$z = (1/N)\Sigma z_j,$$

where u_j, ρ_j and z_j represent individual digitized samples of velocity, density and vertical co-ordinate. N is typically about 2000, which corresponds to an averaging time of roughly 40 s for each value of z. Similarly, root-mean-square quantities are obtained by evaluating

$$u'(z) = [\sum_j (1/N)\,(u_j - \bar{u}(z))^2]^{\frac{1}{2}},$$

and

$$\rho'(z) = [\sum_j (1/N)(\rho_j - \bar{\rho}(z))^2]^{\frac{1}{2}}.$$

These data are then normalized by ΔU and $\Delta\rho$ respectively.

A convenient measure of the vertical extent of the mixing region is provided by an integral thickness, θ_u, defined as

$$\theta_u = [1/(\Delta U)^2] \int_{-\infty}^{\infty} (U_B - \bar{u}(z))\,(\bar{u}(z) - U_T)\,dz.$$

The characteristic integral length scale at the entrance to the test section is θ_i, defined as $\theta_i \equiv \theta_u$ ($x = 1$ cm). One can also define an equivalent density integral scale,

$$\theta_\rho = [1/(\Delta\rho)^2] \int_{-\infty}^{\infty} (\rho_B - \bar{\rho}(z))\,(\bar{\rho}(z) - \rho_T)\,dz.$$

Another quantity which proves to be useful is the probability density function, $P(\rho, z)$, defined by

$$P(\rho, z) = (1/N) \sum_{j=1}^{N} [H(\rho_j - \rho) - H(\rho_j - (\rho + d\rho))],$$

where H is the Heaviside step-function. P defines the percentage of time the density record at a given value of z lies within the window ρ and $\rho + d\rho$.

One final parameter calculated in the data reduction program is a quantity called the mixedness, $M(x, z)$ (Konrad 1976),

$$M(x,z) = \frac{\int_0^T H(\rho - \bar{\rho})\,(\rho_B - \rho)\,dt + \int_0^T H(\bar{\rho} - \rho)\,(\rho - \rho_T)\,dt}{\int_0^T H(\rho - \bar{\rho})\,(\rho_B - \bar{\rho})\,dt + \int_0^T H(\bar{\rho} - \rho)\,(\bar{\rho} - \rho_T)\,dt}.$$

At the vertical location where $\bar{\rho} = \rho_{\mathrm{AV}}$, the mixedness becomes

$$M(x) = [2/\Delta\rho T] \int_0^T [H(\rho - \rho_{\mathrm{AV}})\,(\rho_B - \rho) + H(\rho_{\mathrm{AV}} - \rho)\,(\rho - \rho_T)]\,dt.$$

When fluid is totally mixed in the molecular sense $M(x) = 1$. If, on the other hand, the fluid is completely unmixed, $M = 0$.

3. Flow visualization

3.1. *Initial instability*

The laminar shear region formed immediately downstream of the splitter plate is significantly thicker than the initial density interface. The temporal instability in such a system has been considered analytically by Holmboe (1962) and Hazel (1972). Experimentally, Browand & Wang (1972) investigated the spatial growth characteristics for the case where the density interface is positioned at the midpoint of the sheared region. An important result of these studies is the appearance of several modes of instability, each having a distinct character. Theoretically, for Ri less than about 0·08 the most unstable wave which develops is non-dispersive, and is the stratified analogue of the most unstable mode which occurs in a homogeneous shear layer (Rayleigh mode). For larger values of Ri however, another type of disturbance dominates. This mode (termed the Holmboe mode by Browand & Winant 1973) is dispersive, the degree of dispersion increasing with increasing Richardson number. Inviscidly, there is a range of unstable wave numbers for this mode which exists no matter how large the (maximum) Richardson number becomes. Hazel's numerical

studies show that the Holmboe mode may be generated whenever the thickness of the shear region exceeds the thickness of the density interface by at least a factor of two.

Redekopp (unpublished) has determined stability characteristics when the density interface is shifted away from the centre of the shear region (the case $\epsilon \neq 0$). The appearance of an additional length scale causes the unstable Holmboe mode solutions to bifurcate, forming two non-contiguous unstable regions. Two solutions having distinctly different wavenumbers and comparable amplification rates are now possible. Again, both these solutions are dispersive waves.

Figure 4(*a*) (plate 1) shows the appearance of the initial instability for $Ri = 0{\cdot}075$, $Re = 300$. The fluid is moving from left to right with the bottom layer having the higher velocity. The horizontal lines in the background are 0·5 cm apart, and the vertical lines are separated by 2·5 cm. Dye is introduced at the top and bottom of the sheared region. At this value of Richardson number, the instability is qualitatively similar to the homogeneous case. The evolution of the initial disturbance is to concentrate the existing shear layer vorticity into discrete lumps. This is probably possible because of the almost non-dispersive nature of the most unstable waves for this spatially growing instability. In figure 4(*b*), lines of constant phase are visualized by looking down from above the channel using a shadowgraph. The instability is observed to be quite two-dimensional.

Figure 5(*a*) (plate 2) shows the appearance of the shear layer when the initial Richardson number is about 0·19. Two dye tracers are positioned at the same vertical location in the centre of the shear region, but displaced laterally by 1 cm. The upper dye line exhibits features reminiscent of the lower Ri cases, with the instability acting to spatially concentrate the available vorticity. By contrast, the second tracer shows none of this structure, but rather has the appearance of an interfacial wave. (Figure 7 presents the same case viewed using a shadowgraph. Here we see a preferential entrainment of upper layer fluid into the lower layer, which may be a result of the relative displacement of the initial shear and density profiles.) Observation of the interface from above as in figure 5(*b*) shows the instability to be a complicated mixture of two- and three-dimensional propagating wave trains. Viewing sequences of photographs, there appear to be three distinct sets of waves: (approximately) two-dimensional waves with wavenumbers of about 1·5; waves with wave fronts at angles of about $\pm 30°$ from the stream direction and wavenumbers of about 3·5; and finally waves with wave fronts at angles of $\pm 60°$ from the stream direction and wavenumbers of about 1·7. In the direction of propagation, the wave speeds are respectively 0·5, $-0{\cdot}3$, and 0, where the wave speed is defined as

$$Cr = [(\text{distance travelled by wavefront})/\Delta t - \bar{U}]/(\Delta U/2).$$

The different families of waves originate in different spanwise locations, and this may be due to slight spanwise irregularities in the thickness of the shear layer. Small lateral variations in h_i of the order of $\pm 6\,\%$ do exist, and it must be concluded that the nature of the instability is very sensitive to small, local changes in the Richardson number. The range near $Ri \approx 0{\cdot}2$ may be particularly sensitive, for limited observation at higher Richardson numbers show the instability to be more two-dimensional and much less confused. The existence of oblique, dispersive waves in the range $0 < Ri < 0{\cdot}2$ is not inconsistent with available theory, but at present, the theory is not sufficiently developed to allow detailed comparisons.

3.2. *Active turbulence; collapse and relaminarization*

For initial Richardson numbers less than about 0·15, an active turbulent growth region follows the instability and is characterized by the presence of the large, quasi-organized vortical structures so familiar in the unstratified mixing layer, and by the superposition upon this framework of random, smaller scale irregularities (figure 6, plates 3–5). In some respects the flow may be regarded as turbulent once these large-scale vortical features have become well developed. The continued growth of the turbulent region, for example, depends primarily upon the interactions of these large scale features and hardly at all upon the presence or absence of smaller scales of irregularity. Smaller scale irregularities are produced first in the vortical core regions. The production of small scales is promoted by the interactions between the large-scale features, but even at slightly higher Richardson numbers, when these interactions are largely absent, the core regions still become irregular at small scales. The way in which surrounding fluid is entrained by the core regions (sketched in figure 18) creates local regions of static instability, and this probably aids in the process of fine-scale generation.

Typically, these large turbulent concentrations of vorticity undergo a series of interactions like the one shown in figure 6(*b*). These photographs were obtained using a 16 mm film camera towed at the mean convection speed $\bar{U}$, so that roughly speaking it was always viewing the same patch of fluid. Most often, two neighbouring structures pair to form a single, larger structure. Each time the interaction occurs, the mixing layer is substantially thickened, and the average spacing between the structures is roughly doubled. At some downstream point however, the process is halted, and the large-scale structure fragments and disappears. The turbulent fluid in these structures becomes more or less uniformly distributed within the vertical confines of the mixing layer. Beyond this point, the turbulent region may actually decrease in thickness, and it is clear that the turbulence is no longer active. The smaller scale features take on a striated appearance under the straining of the flow. Figures 6 (*i*)–(*j*) (x = 25–45 cm) represents the point of maximum mixing layer thickness prior to the disappearance of the large-scale structure.

The disappearance of the large vortices and the inability of the resultant flow to remain actively turbulent, even at much smaller scales, is the most important single observation. It emphasizes the crucial nature of the large-scale structure in the maintenance of active turbulence, and also illuminates the mechanism by which a statically stable density difference, no matter how small, acts ultimately to destroy the turbulence. A simple physical explanation for the effect of stable stratification (but one which will need further elaboration) is that the flow induced by the vortical regions raises heavy fluid and depresses light fluid, as in figure 18. As the size of the vortices grows, a point is reached for which there is insufficient energy available to perform this task. Rather than equilibrate in amplitude, the entire turbulent structure is destroyed.

A different sequence occurs at values of the initial Richardson number larger than Ri = 0·15, but the end result is similar. Figure 7 (plates 6 and 7) shows a series of photographs at various downstream positions for an initial Richardson number of 0·2. The interfacial waves which are produced initially continue to grow in amplitude and eventually break at the crest. The crests are always initially associated with the high speed stream. (If the top layer is made to move faster, the waves will peak upward

instead of downward.) Breaking consists of ejection of low speed fluid (in this case lighter fluid) into the high speed side (heavier fluid). As noted earlier, this process is much more three dimensional and much less violent than at lower Richardson numbers. Significant wave motions still exist at the end of the channel, figure 7(*h*), and, although the flow is clearly relaxing towards a laminar state, this is never quite achieved in the present apparatus.

For initial Richardson numbers greater than 0·2, the process is qualitatively similar. Wave breaking in the apparatus is eventually suppressed at Richardson numbers of about 1·0, but this cessation is probably related to the relatively low value of the Reynolds number required to achieve large Ri. Reynolds number effects can be expected to become more important at high Richardson number because the growth rates are lower. The inviscid linear theory suggests that interfacial waves can always be produced having positive growth rates. For large enough Reynolds number, the amplitudes of these waves would presumably also be limited by waves breaking.

4. Experimental results

4.1. *Integral length scales*

Measurements of mean velocity and density are used to calculate θ_u and θ_ρ for the cases listed in table 1. Figure 8(*a*) presents θ_ρ/θ_i as a function of x/θ_i for fixed Re and Ri between 0·05 and 0·2. For low values of the initial Richardson number, one can identify two distinct regions of the flowfield which are, in some sense, separable. In the initial turbulent growth region, the shear layer grows by entrainment of fluid through vortex formation and pairing. A least-squares fit straight line gives a slope of $0{\cdot}0177 \pm 0{\cdot}001$, which compares with $\theta_u \approx 0{\cdot}019 \pm 0{\cdot}002$ for the high Reynolds number, homogeneous mixing layer at the same $\Delta U/\overline{U}$. This active turbulent region extends to the point of maximum shear layer thickness; roughly $x/\theta_i = 300$–450, depending upon the value of Ri. The spatial extent of the linear growth region is sensitive to Richardson number because an increase in buoyancy destroys the large-scale structures at positions closer to the shear layer origin. Beyond this point, the large-scale entrainment processes are suppressed and the mixing layer collapses and approaches a non-turbulent state. This relaxation or relaminarization region extends from the maximum thickness state to the end of the channel.

As the initial Richardson number is increased beyond about 0·125, the growth departs from this previous description. There is practically no initial turbulent growth region. The layer is much thinner, and instead of attaining a well-defined maximum there is a more prolonged, gradual increase in thickness. This distinction between the low and high Richardson number result is traceable again to the two possible initial modes of instability. The more gradual increase in θ_ρ beyond $x/\theta_i = 200$ is also a result of the persistence of breaking interfacial waves which continues for distances of $x/\theta_i \approx 700$–1000.

The measurements of θ_u/θ_i as a function of longitudinal co-ordinates are shown in figure 8(*b*). The variations of θ_u are more complicated, and the results are not as easily interpreted. In the early stages of mixing, the growth rate of θ_u compares well with that of the unstratified mixing layer, particularly for the four smallest initial Richardson numbers. However, θ_u continues to grow beyond the point of maximum θ_ρ. Part of the reason for this difference is that the mean velocity profiles do not remain

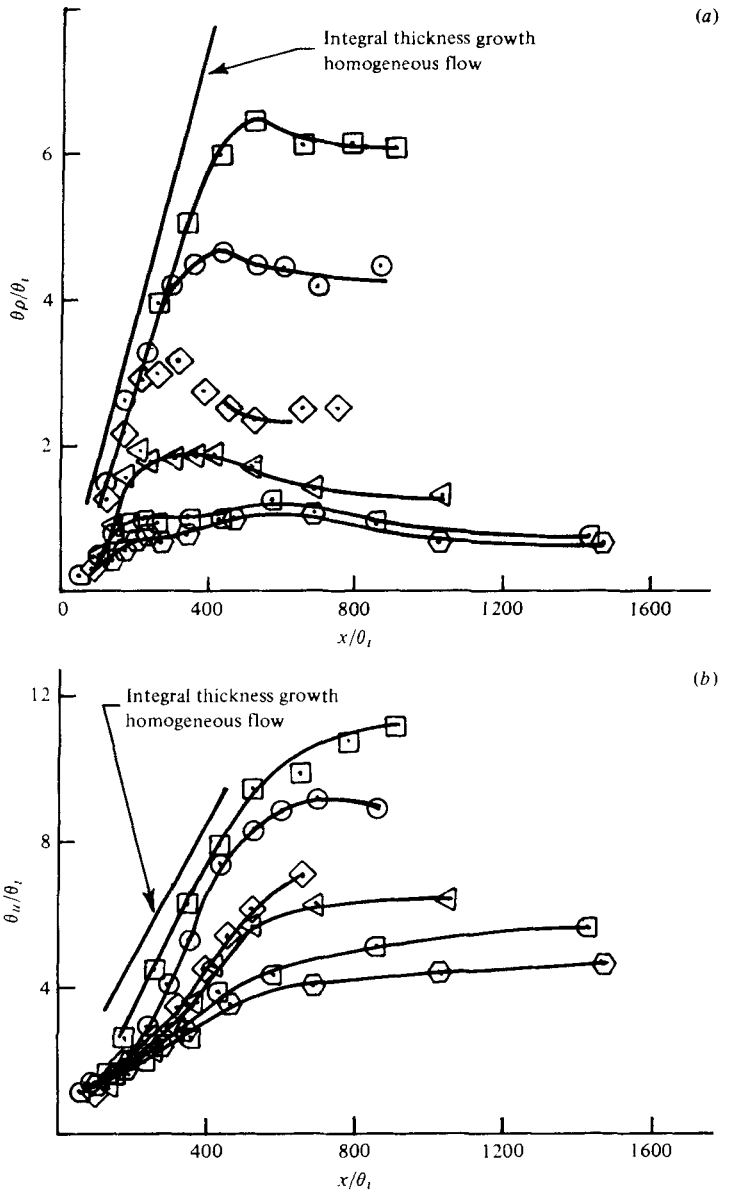

FIGURE 8. Density integral thickness (*a*), and velocity integral thickness (*b*), *vs.* downstream distance for various initial Richardson numbers. □, $Ri = 0{\cdot}05$; ○, $Ri = 0{\cdot}075$; ◇, $Ri = 0{\cdot}1$; ◁, $Ri = 0{\cdot}125$; ▢, $Ri = 0{\cdot}15$; ⬡, $Ri = 0{\cdot}2$; $Re = 300$. Lines labelled integral thickness for homogeneous mixing layer' use the results summarized by Brown & Roshko (1974).

similar in shape through and beyond the point of maximum θ_ρ (see figure 10). This causes a change in θ_u, which is not (necessarily) related to a physical thickening of the layer.

4.2. *Mean velocity and mean density profiles*

Figure 9 presents profiles of mean density $\bar{\rho}(z)$ for several values of x/θ_i for the case $Ri = 0{\cdot}075$, $Re = 300$. The data at each station have been shifted so that $\bar{\rho} = \rho_{\mathrm{AV}}$ at

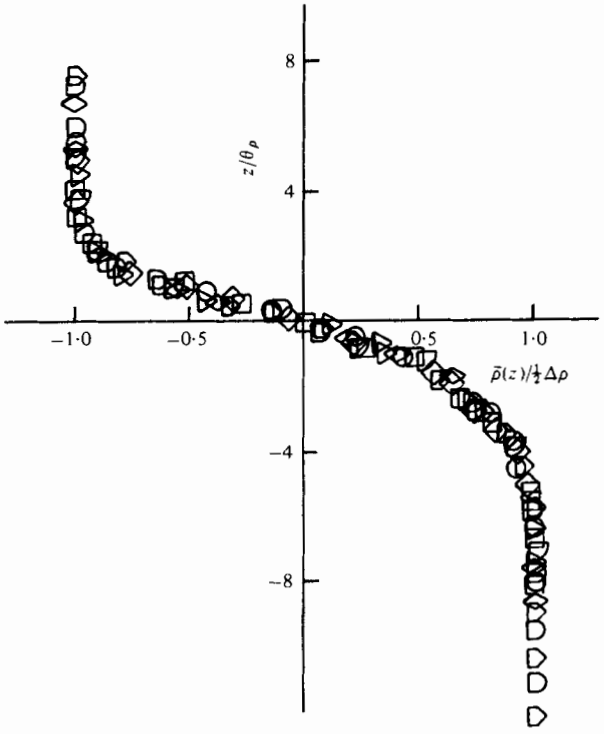

FIGURE 9. Mean distribution of density for $Ri = 0{\cdot}075$, $Re = 300$. Downstream distances x/θ_i are: ▽, 115; ▷, 173; ◇, 229; ○, 287; □, 343; ⬠, 430; ▷, 516; ◇, 862.

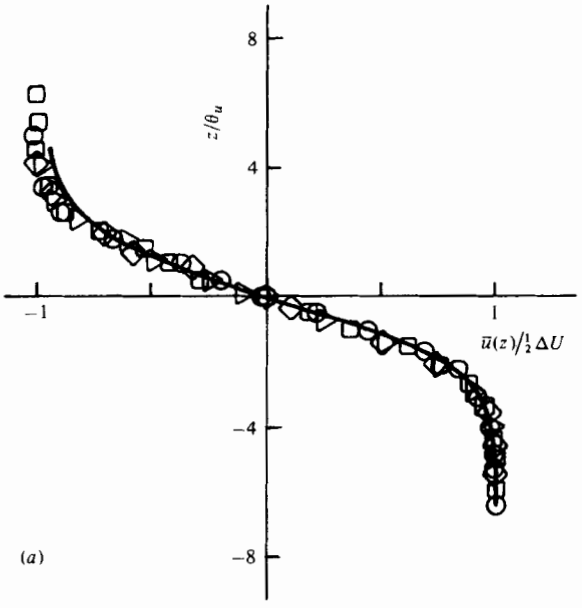

FIGURE 10(a). For legend see next page.

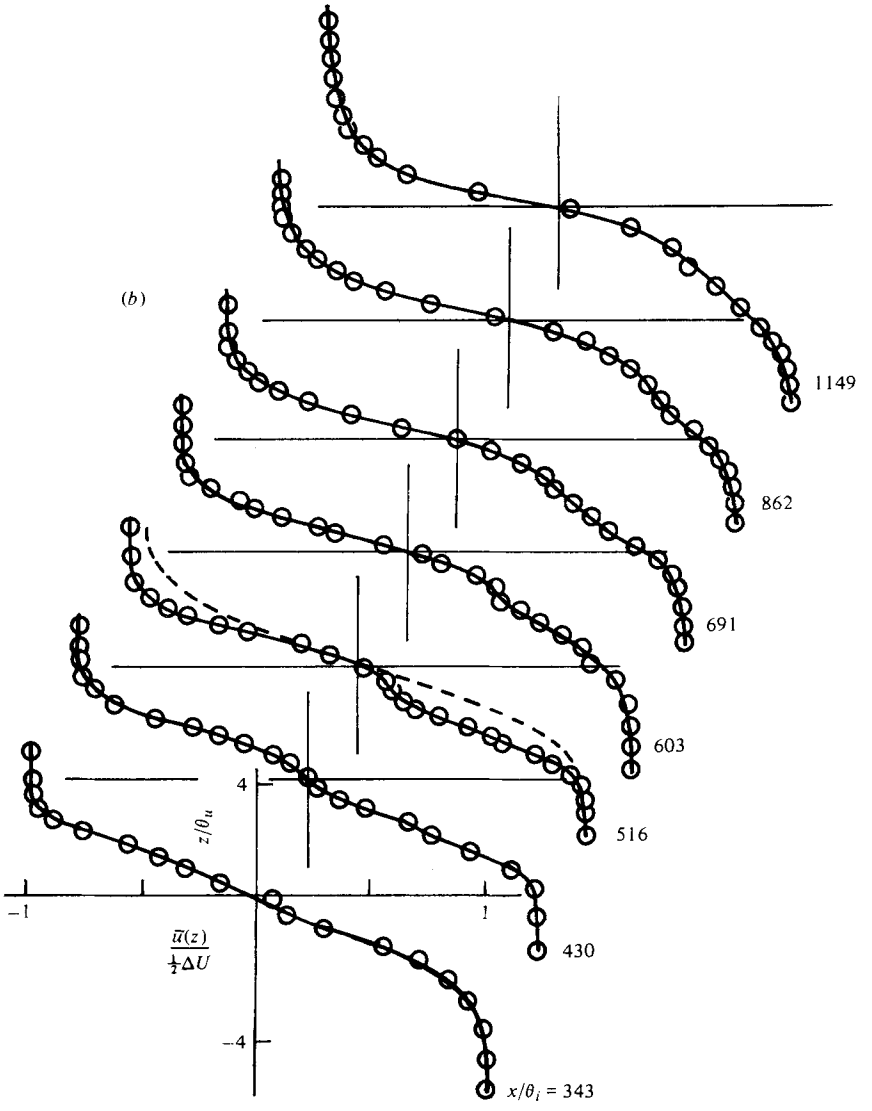

FIGURE 10. Mean distribution of velocity for $Ri = 0{\cdot}075$, $Re = 300$. (*a*) Downstream distances x/θ_i are: □, 115; ○, 173; ◇, 229; ▷, 287. ——, Liepmann & Laufer (1947). (*b*) Downstream distances as indicated, – – –, Leipmann & Laufer (1947).

$z = 0$. The normalized density profiles are similar over the entire downstream range, $115 < x/\theta_i < 860$. This is quite surprising since the physical appearance of the flowfield varies significantly over this range of x. It must be concluded that the mean density profiles are insensitive to the different physical processes which are important in certain regions of the flow. Figure 10 presents similar data for the normalized velocity profiles $\bar{u}(z)$. For $x/\theta_i < 300$ (figure 10*a*), the mean velocity distributions possess similarity. The solid curve is the data obtained by Liepmann & Laufer (1947) for a homogeneous mixing layer.

The mean velocity profiles downstream of $x/\theta_i = 300$ are shown in figure 10(*b*). The

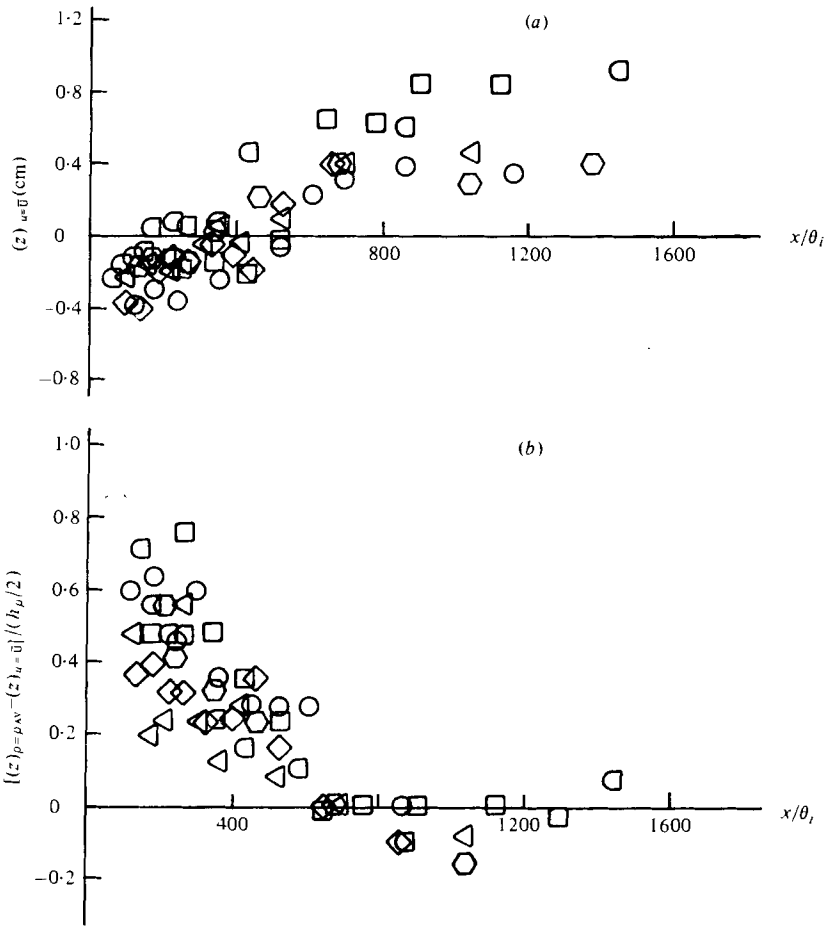

FIGURE 11. (*a*) Vertical location (referred to the position of the splitter plate) of the point in the mean velocity profile where $\overline{u}(z) = \overline{U}$. (*b*) Difference in vertical position of $\overline{u}(z) = \overline{U}$ and $\rho(z) = \rho_{AV}$. The symbols are the same as in figure 8.

shape of the profiles is quite distinct from the upstream data. Also, no similarity is established. The abrupt change in profile shape is related to the dominance of buoyancy forces, and to the redistribution of momentum produced by the collapse of the large-scale structure.

Two other pieces of information associated with the averaged profiles is presented: the location of the point where the velocity is equal to the mean velocity, figure 11 (*a*); and the location of the corresponding point in the density distribution, figure 11 (*b*). For $x/\theta_i > 600$, the points where $\rho = \rho_{AV}$ and $u = \overline{U}$ are coincident.

4.3. *Density and velocity fluctuations*

The maximum values of the r.m.s. density and velocity fluctuations at each downstream position are presented in figure 12 for several values of the initial Richardson number. (Note that $\rho'/\Delta\rho$ has an absolute maximum value of 0·5.) Beyond the point of maximum thickness, all of the data collapse to a single curve provided $Ri < 0{\cdot}125$, and show a decay proportional to $(x/\theta_i)^{-\frac{3}{4}}$. This is the same rate of decay found for

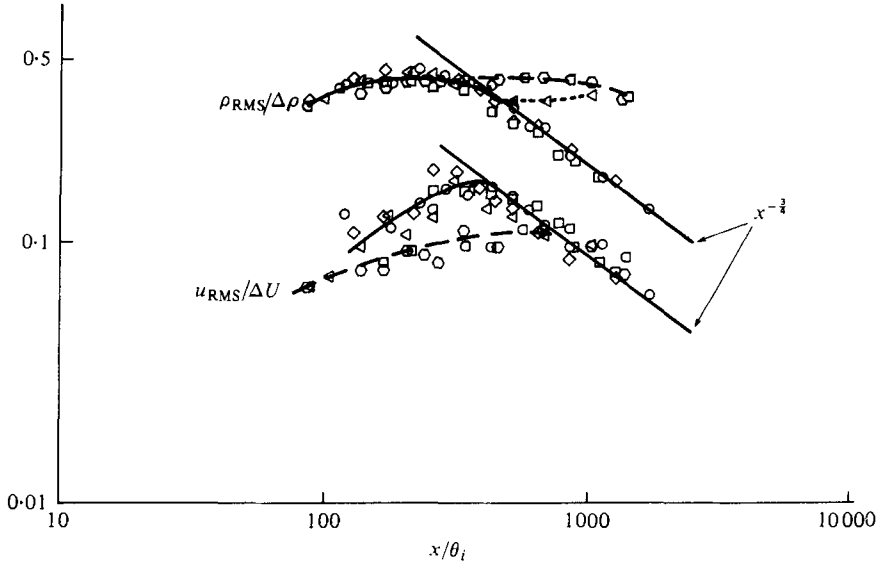

FIGURE 12. Root-mean-square velocity and density fluctuations with downstream distance. The symbols are the same as in figure 8. ——, $Ri < 0{\cdot}125$; ----, $Ri = 0{\cdot}125$; --, $Ri > 0{\cdot}125$.

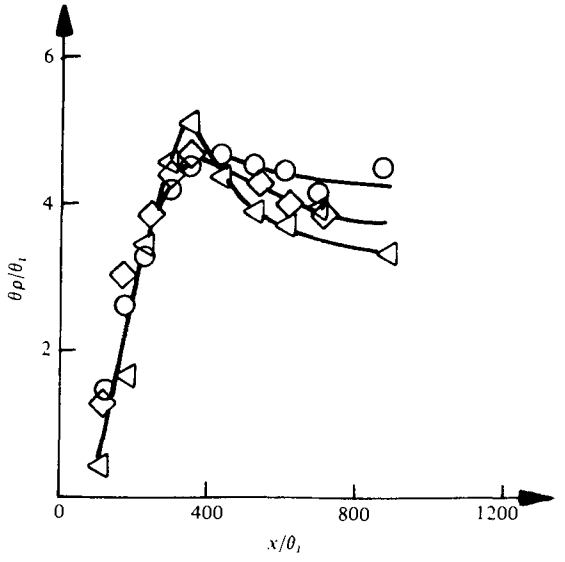

FIGURE 13. Density integral thickness as a function of downstream distance, $Ri = 0{\cdot}075$. Initial Reynolds number and corresponding maximum Reynolds number are: ◁, $Re = 200$, $Re_{MAX} = 1000$; ◇, $Re = 250$, $Re_{MAX} = 1200$; ○, $Re = 300$, $Re_{MAX} = 1450$.

scalar quantities in isotropic grid turbulence, as measured by Lin & Pao (1979) and discussed by Hinze (1959, p. 237). Again the different character of the high Richardson number data is evident.

Similar data is presented for the velocity fluctuations. The data in the relaminarization region fall roughly on a single curve for all Richardson numbers. A solid line with slope $-\frac{3}{4}$ fits the data as well as any, although there is too much scatter and too little data to draw much of a conclusion.

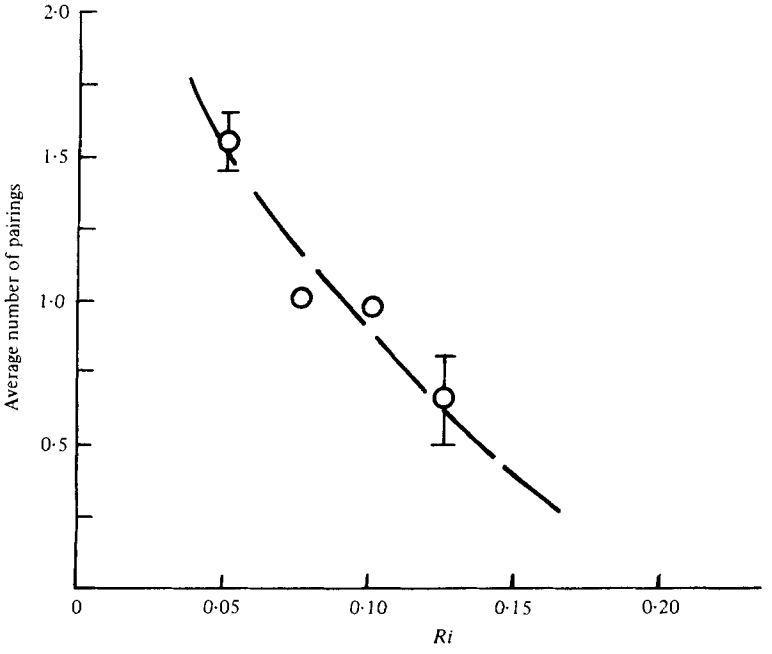

FIGURE 14. Average number of pairings *vs.* initial Richardson number, $Re = 300$. Bars indicate approximate confidence in measurements.

4.4. *Variation of Reynolds number*

To what extent are the growth and decay regions sensitive to changes in Reynolds number? One might anticipate a minor role for viscosity in the turbulent growth region, since here the dynamics are controlled by large-scale structures which are not sensitive to changes in Reynolds number. However, viscosity and diffusion of salinity will probably both be important in the relaminarization region. Figure 13 gives the value of the density length scale, θ_ρ, as a function of downstream distance for several Reynolds numbers with the initial Richardson number fixed at $Ri = 0{\cdot}075$. In the turbulent growth region, all of the data show roughly the same rate of growth, and all compare well with unstratified high Reynolds number mixing-layer data. One also sees that the maximum thickness and the location of the maximum thickness point are both relatively insensitive to Reynolds number – at least over the limited range investigated. In the relaminarization region, though, a definite Reynolds number effect is noted, θ_ρ relaxes to smaller asymptotic values as Re decreases.

5. Discussion

5.1. *Turbulent growth to maximum thickness*

The turbulent growth regime is dominated by the formation and interaction of discrete vortical structures, or vortices. Much information about this pairing process may be obtained by analyzing the spatial and temporal history of the vortices. For example, data taken from a 16 mm film for the case $Ri = 0{\cdot}05$, and displayed in an x, t plot shows that the first pairing occurs at a mean location of $x/\theta_i = 170$ with a standard deviation of $\pm$ 90. Virtually all the vortices (97 %) undergo at least one pairing, and often another

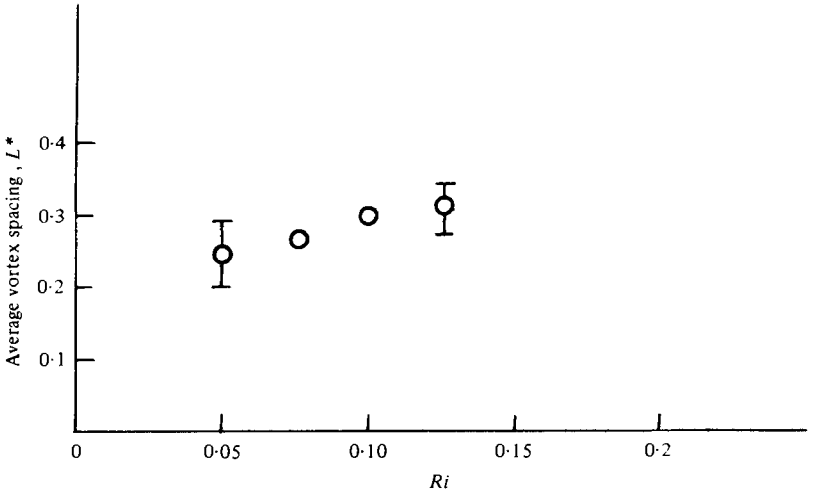

FIGURE 15. Average vortex spacing, L^*, at point of maximum mixing layer thickness versus initial Richardson number $Re = 300$. $L^* = g\Delta\rho L/\pi\rho_{AV}(\Delta U)^2$, where L = physical vortex spacing. Bars indicate approximate confidence.

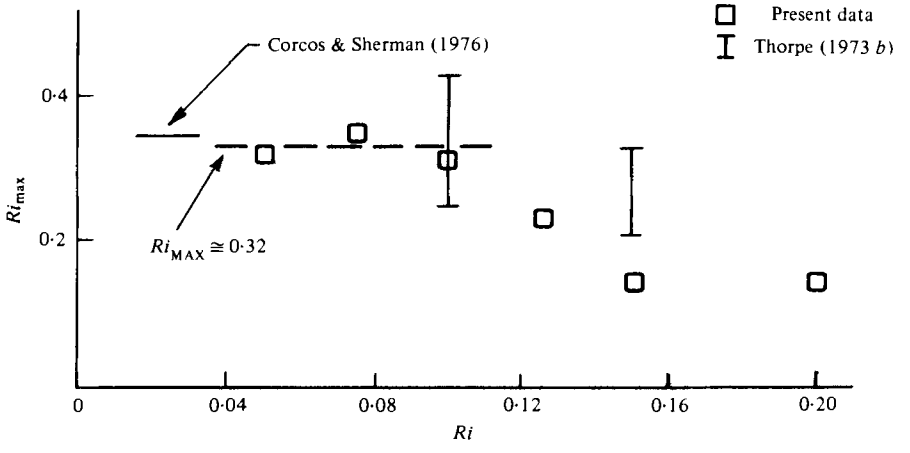

FIGURE 16. Richardson number at point of maximum mixing layer thickness,

$$Ri_{MAX} = g\Delta\rho h_{MAX}/\rho_{AV}(\Delta U)^2$$

vs. initial Richardson number for $Re = 300$. The relation $h_{MAX} \approx 5(\theta_\rho)_{MAX}$ is used.

interaction occurs. The mean location of this second pairing is $x/\theta_i = 350 \pm 180$. The second pairing is a much more intermittent phenomenon, with only 56 % of the initial vortices experiencing more than a single interaction prior to achieving the maximum thickness state. One may quantify the average number of pairings by considering the average rate at which vortices convect past the point of maximum thickness relative to the rate at which they are formed initially. Because of the intermittency of pairing, the average number of pairings is not necessarily an integer. The average number of pairings is shown plotted in figure 14 as a function of Ri. Beyond $Ri = 0{\cdot}125$, buoyancy forces have nearly suppressed the pairing process completely.

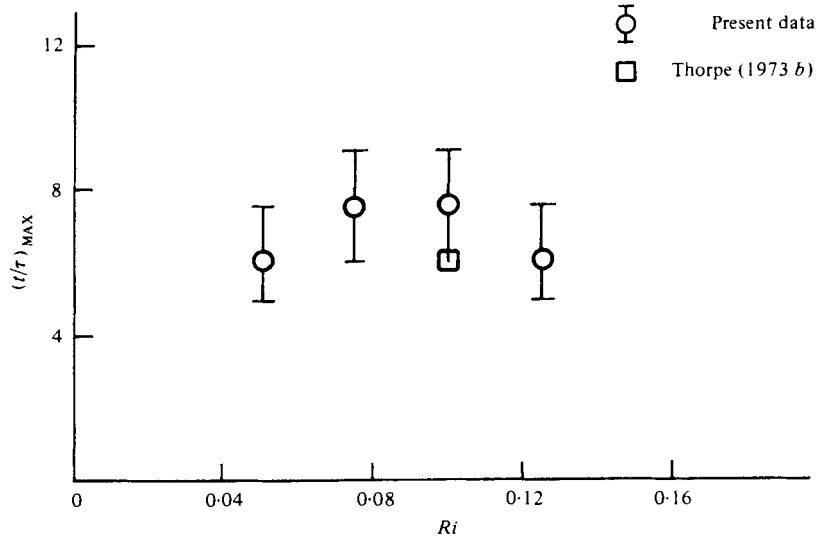

FIGURE 17. Time to point of maximum mixing layer thickness *vs.* initial Richardson number for $Re = 300$. The normalizing time $\tau = \rho_{AV}\,\Delta U/g\Delta\rho$.

The average vortex spacing at the point of maximum amplitude can also be determined. Let

$$L^* = g\Delta\rho L/\pi\rho_{AV}(\Delta U)^2,$$

where L is the average distance between adjacent vortex cores. (The $1/\pi$ factor is introduced for consistency with the notation of a theoretical model to be discussed subsequently.) The non-dimensional spacing at the point of maximum thickness is shown in figure 15. This non-dimensional spacing is close to 0·3 and only changes by 20 % for a threefold increase in Richardson number.

One may further quantify conditions at the maximum thickness by examining the value of the Richardson number, Ri_{MAX} defined as

$$Ri_{MAX} = g\Delta\rho h_{MAX}/\rho_{AV}(\Delta U)^2,$$

where h_{MAX} is the maximum slope thickness of the mean density profile. Figure 16 presents the value of Ri_{MAX} as a function of initial Richardson number. (h_{MAX} is determined from the θ_ρ data shown in figure 8*a* by use of the relation $h_{MAX} \approx 5\theta_\rho$). For $Ri \leqslant 0{\cdot}1$, Ri_{MAX} has the constant value of $0{\cdot}32 \pm 0{\cdot}02$. This result is consistent with the data of Thorpe (1973*b*), whose experimental conditions were somewhat different from the present experiment. The maximum Richardson number decreases steadily to a value of approximately 0·15, as the initial Richardson number increases beyond 0·1. The process of interfacial wave breaking at high Richardson numbers is very different from the vortex pairing process at low initial Richardson numbers.

The length of the turbulent growth region can also be established in a useful non-dimensional form. Since the maximum thickness state is a direct result of the growing importance of buoyancy, any non-dimensionalization must include the factor $g\Delta\rho/\rho_{AV}$. The distance x_{MAX} to the location of the point where θ_ρ is a maximum, is converted to a time by convecting with the mean speed, $\bar{U}$. This time is normalized by the buoyancy time scale, $\tau = \Delta U/(g\Delta\rho/\rho_{AV})$ to give a non-dimensional time, $(t/\tau)_{MAX}$, which locates

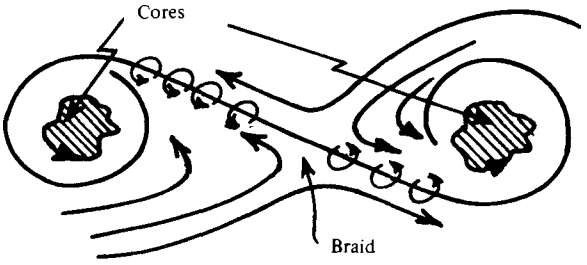

FIGURE 18. Schematic diagram of vortex core regions separated by vorticity producing braid.

the maximum thickness point. The results are shown in figure 17 for $Ri \leqslant 0{\cdot}125$. (For $Ri > 0{\cdot}125$, no well-defined location exists for the maximum thickness state.) The duration of the turbulent growth region is limited to about 6–7 non-dimensional time scales, independent of the initial Richardson number. The results of Thorpe (1973*b*) are in good agreement with this conclusion.

5.2. *Experimental comparisons with the model of Corcos & Sherman* (1976)

Recently, Corcos & Sherman have developed a model to explain how buoyancy limits the maximum thickness of the mixing layer. The sketch in figure 18 shows two vortical core regions which produce a highly strained region between, often referred to as the braid. According to the model, vorticity is produced baroclinically within the braid region and transported to the vortex cores. Within the core region vorticity is destroyed through the entrainment of ambient fluid which, by lifting heavy fluid, and depressing light fluid, produces a torque that is in an opposite sense to that of the fluid rotation (vorticity). In the absence of interactions, the growth of the vortex core regions will equilibrate at a maximum amplitude such that the rate of vorticity transport out of the braid is just balanced by baroclinic generation within the braid. This limiting amplitude or thickness is predicted to be

$$Ri_{\mathrm{MAX}} = \tfrac{1}{2}\pi L^*(1-L^*),$$

where Ri_{MAX} and L^* have previously been defined. The circulation about the core, expressed as a fraction of the total circulation (a constant), is given by

$$\Gamma_c/\Gamma = 1-L^*.$$

The non-dimensional time to achieve maximum thickness is also a function of L^* only.

The *observed* value of the vortex core spacing at the point of maximum thickness is about $L^* \approx 0{\cdot}3$ for initial Richardson numbers below 0·125. Using this value of L^*, Corcos & Sherman would predict a value of $Ri_{\mathrm{MAX}} = 0{\cdot}33$ which agrees well with the experimentally determined value of $0{\cdot}32 \pm 0{\cdot}02$. The theory further predicts a value for the core circulation, $\Gamma_c/\Gamma \approx 0{\cdot}7$; at maximum thickness, 70 % of the total circulation resides in the core regions and 30 % resides in the braid regions between the cores.

This model allows for vortex growth by entrainment, but *does not* include the observed nonlinear (pairing) interactions between adjacent vortex structures. It could be argued that the model does describe conditions for equilibrium between baroclinic generation in the braid and destruction in the core, and should adequately represent vortex growth between pairings. However, the model does not explicitly include the dynamics of vortex interaction and there is no *a priori* way to theoretically choose the

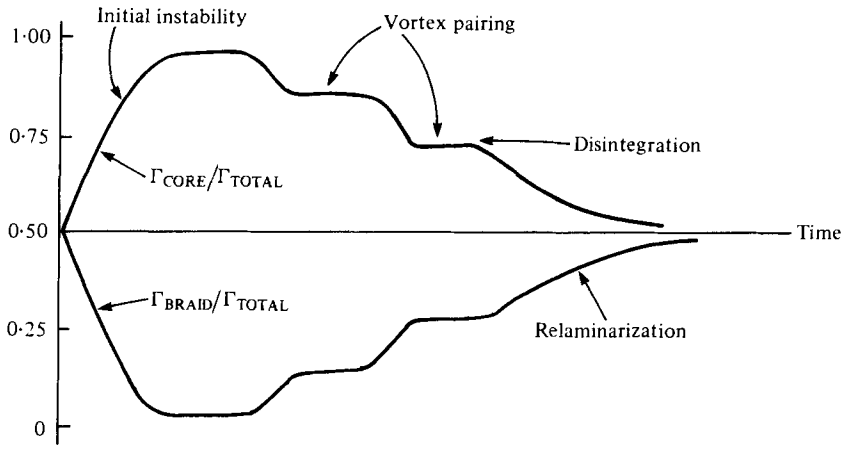

FIGURE 19. Schematic diagram of core and braid circulation during the time evolution of the mixing layer.

appropriate value of L^* (and, hence Ri_{MAX}) which characterizes the maximum thickness state. In our opinion, the relative distribution of circulation between core and braid is the significant feature of the maximum thickness state. The experimental results suggest that vortex pairing can proceed until the circulation about the core regions falls below (approximately) 70 %; then the large-scale vortical interactions can no longer be maintained and the mixing layer disintegrates. A sketch of the time history of the circulation about the core and braid is presented in figure 19.

Initially, the vorticity is uniformly distributed in the laminar shear flow, and, after collapse of the large structure, it is again uniformly distributed. Thus, the circulation about core and braid must begin and end at the value of 0·5. The initial instability produces a large increase in core circulation and a corresponding decrease in circulation around the braid. Core circulation is larger for smaller values of the initial Richardson number. Pairing proceeds and the mixing layer thickens while the core circulation falls by steps toward the value 0·7 – the termination of the pairing process and the disintegration of the large-scale structure. This empirical addition to the theoretical result of Corcos & Sherman accounts for the pairing process and eliminates the need to determine L^*. Any L^* less than (approximately) 0·3 is a theoretically acceptable spacing at some stage of the process, but the mixing layer will grow until $L^* \approx 0{\cdot}3$, $Ri_{MAX} \approx 0{\cdot}32$. (The theoretically predicted time to attain this maximum thickness is about 4τ to 5τ which is also in reasonable agreement with the experimental results although the pairing is not explicitly considered!)

5.3. *Turbulent entrainment and molecular diffusion*

One of the most important products of the turbulent event is the resultant irreversible mixing of solute which takes place. A distinction must be made between fluid entrained into the mixing layer, which occurs as a result of the organized motions of the large-scale vortices, and fluid which is mixed to molecular scales. A parcel of fluid can have its density altered only as a result of molecular diffusion, and this change in density does not occur instantaneously at the time the fluid parcel enters the layer. Rather, a

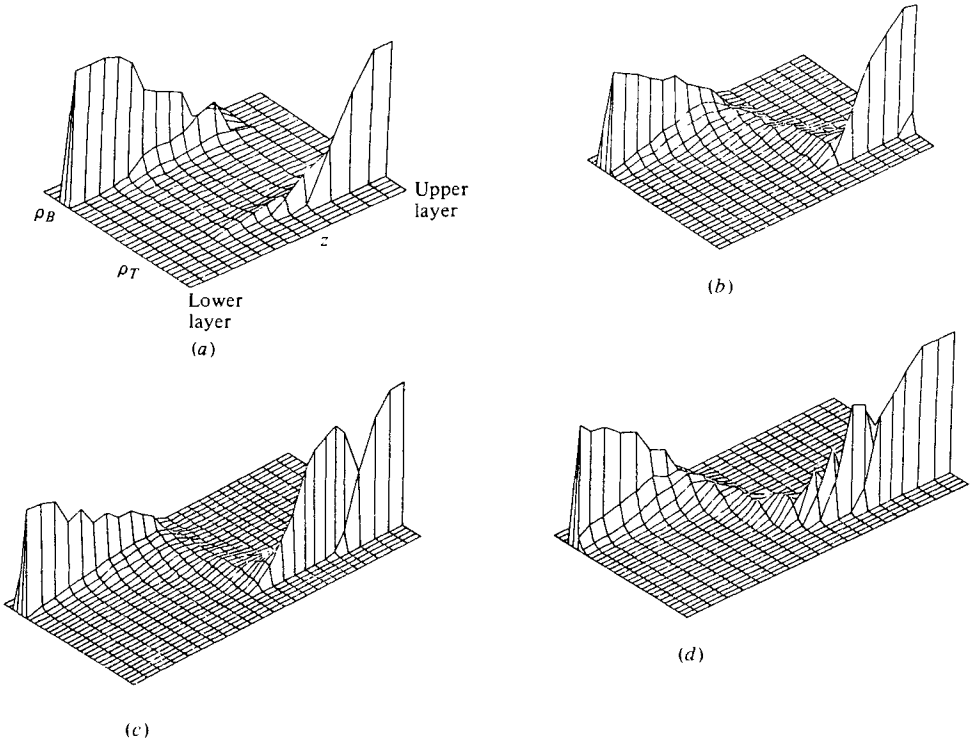

FIGURE 20. Isometric projections of the density probability density function, P, for $Ri = 0{\cdot}075$, $Re = 300$. (*a*) $x/\theta_i = 170$; (*b*) $x/\theta_i = 430$; (*c*) $x/\theta_i = 690$; (*d*) $x/\theta_i = 1150$.

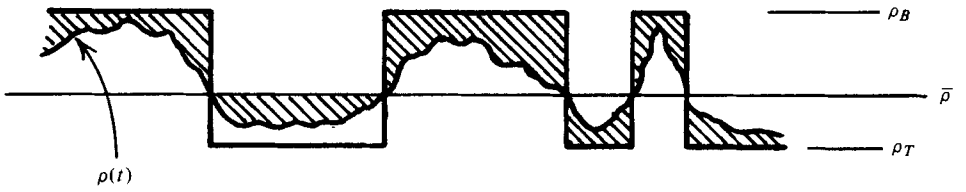

FIGURE 21. Sketch of instantaneous density trace as a function of time.

gradual diffusive exchange takes place, which is only made efficient in the turbulent flow by the enormously increased surface area available to the diffusing constituents.

The extent of molecular mixing can be visualized by isometric plots of the probability density function (of density). An example is shown in figure 20, for four downstream locations at an initial Richardson number of 0·075. At the first location, the probability distribution is bimodal; the fluid entrained into the layer has a very small probability of having a density other than that of the top and bottom layers. In effect, the local instantaneous density swings alternately between ρ_B and ρ_T. The mean density measures the relative proportion of time spent in each state. The distribution at the second location, close to the point of maximum mixing-layer thickness, still shows relatively little molecular mixing. At subsequent downstream locations, the original bimodal structure gradually evolves into a single, peaked probability density. At the final station, for any value of z within the mixing region, the probability appears

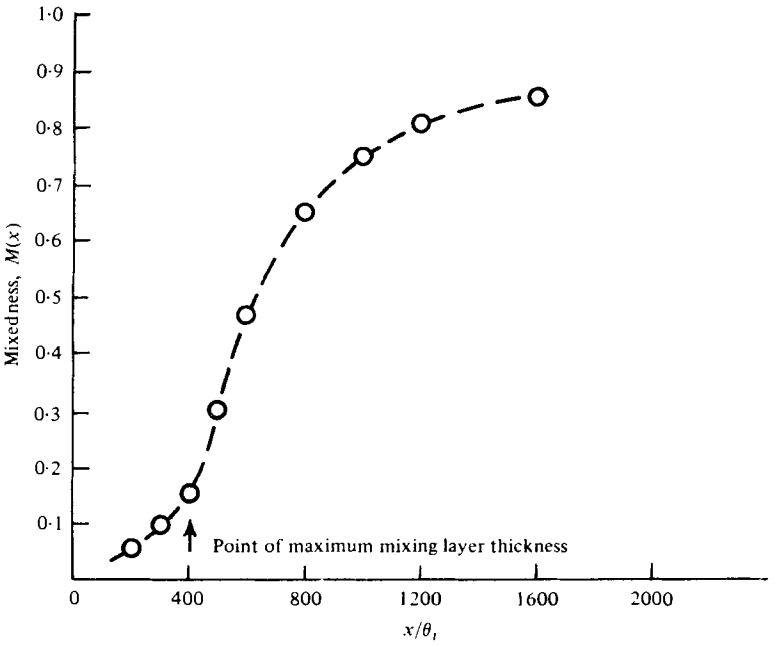

FIGURE 22. Degree of mixedness, $M(x)$ (defined in §2.2) as a function of downstream distance for $Ri = 0{\cdot}075$, $Re = 300$. For complete mixing $M(x) = 1$; for no mixing $M(x) = 0$.

to be roughly symmetric about the maximum value. Here the probability peak approximately describes the mean density profile, and the density fluctuations are closely concentrated about this mean distribution.

One relative measure of the degree of the molecular mixing is embodied in the mixedness parameter defined in §2.2. In the sketch below, figure 21, a density time trace is illustrated. The superimposed square wave is the form of the density variation if no mixing has occurred. The mixedness is defined as the ratio of the hatched area to the total area under the square wave. Mixedness is zero when no molecular mixing has occurred, and is unity when all fluctuations are absent and the density assumes the value of the mean density, $\bar{\rho}(z)$. (In reality a density probe measures density as an average over some small fluid volume which depends upon the size of the probe. Such a probe can make no inference about mixing on scales smaller than this resolving volume.)

The mixedness measured by the microprobe along the centre-line of the channel, where $\bar{\rho} = \rho_{\mathrm{AV}}$, is shown in figure 22 for an initial Richardson number of 0·075. The results are similar to those obtained from the probability distributions. Mixedness is initially low and rises rapidly only after the collapse of the large-scale structure. One possible explanation for the initially low value of mixedness is that, in the actively turbulent region, fluid is entrained at such a rapid rate that there is a preponderance of unmixed fluid. The Reynold's numbers are relatively low, and the smallest scales present in the active region are much larger than one would estimate using an equilibrium, homogeneous turbulence model. With the same probe used to measure the mixedness, the longitudinal Taylor microscale was measured as a function of

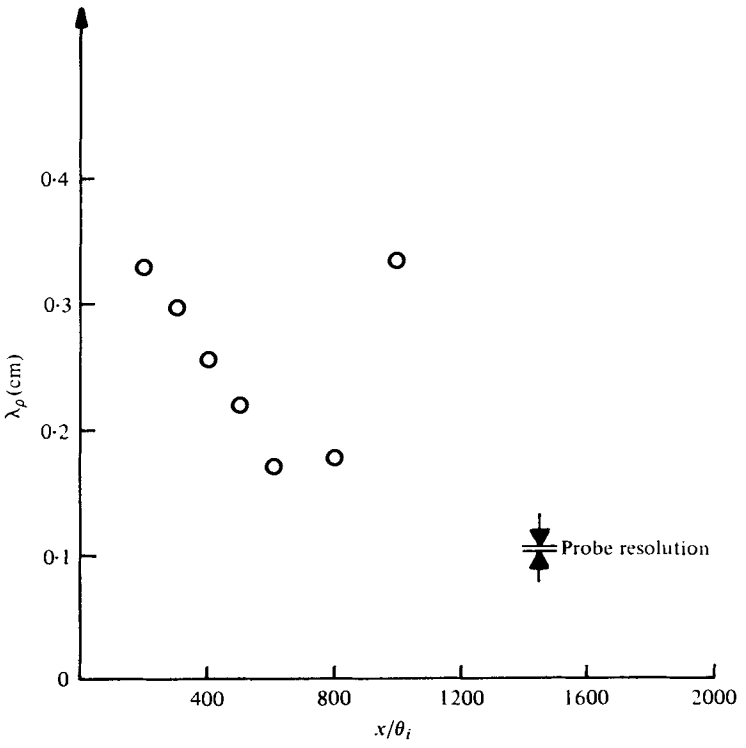

FIGURE 23. Centre-line value of density microscale, $\lambda_\rho = [\overline{2\rho'\overline{U}^2}/(\overline{\partial\rho'/\partial t)^2}]^{\frac{1}{2}}$, *vs.* downstream distance for $Ri = 0{\cdot}075$, $Re = 300$.

downstream distance along the centre of the mixing region, figure 23. (The linear dimension of the resolving volume for this probe is of the order of 0·05 mm and is consequently much smaller than the scales being measured.) The actively turbulent region is characterized by a decreasing microscale with increasing downstream distance. For a self-similar flow, the microscale should grow with increasing downstream distance. This opposite behaviour suggests insufficient time is available to establish similarity for the small scales.

Downstream from the point of maximum thickness, the turbulence decays and the microscale begins to increase. Mixedness also increases rapidly in this region (figure 22) because the entrainment of new fluid has virtually ceased. Now there is competition between molecular mixing (diffusion) and the tendency for unmixed fluid to return to the layer in which it originated. Examples of the instantaneous vertical distribution of density at $x/\theta_i \approx 1000$ are shown in figure 24 (plate 8) for a Richardson number of 0·075. The data were obtained by rapidly traversing the mixing layer with a conductivity probe and simultaneously taking a photograph. Although small-scale microstructure is still present as a result of the turbulent event, on the whole the density variation is rather smooth with no sharp discontinuities separating well-mixed layers. A measure of the thickness of the mixed region, and consequently of the total mixing which has taken place upstream, is given by an integral of the mixedness;

$$\delta = \tfrac{1}{2}\int M(z)\,dz, \quad \text{with} \quad \bar{\rho} = \rho_{\mathrm{AV}}, \quad \rho(z,t) = \bar{\rho}.$$

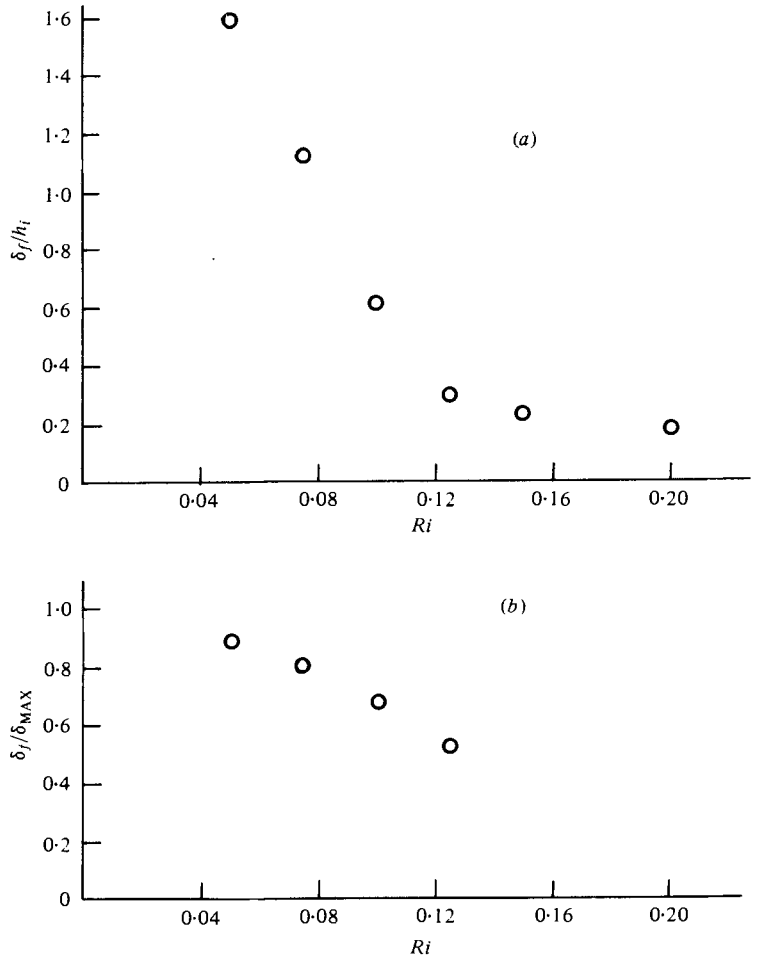

FIGURE 25. Integral thickness of the final mixed region, δ_f, normalized by (*a*) h_i, and (*b*) δ_{MAX}, as a function of the initial Richardson number. $Re = 300$.

An exact determination of the total mixing requires a knowledge of the position of the dividing streamline at the downstream location. Insufficient information is available to locate the dividing streamline, and the computation here centres the distribution at the point where $\bar{\rho}(z) = \rho_{AV}$. The value of δ is now underestimated; when the profile is anti-symmetrical about the average density, δ represents the lowest possible value of mixing at each Richardson number.

The values of δ_f/h_i at the last downstream location $x/\theta_i \approx 1000$–1400, are shown plotted in figure 25(*a*) as a function of the initial Richardson number. The amount of mixed fluid first decreases rapidly with increasing Richardson number, primarily due to the decreasing amount of entrainment in the turbulent growth region, and then levels off. The diminishing slope at larger values of Richardson number probably reflects the transition to wave breaking; a different process from the roll-up and collapse at lower Ri. Figure 25(*b*) shows the Richardson number dependence of δ_f/δ_{MAX}, where δ_{MAX} is the value of δ at the point of maximum mixing layer thickness. The general decline of δ_f/δ_{MAX} with increasing Ri can be understood as a greater tendency

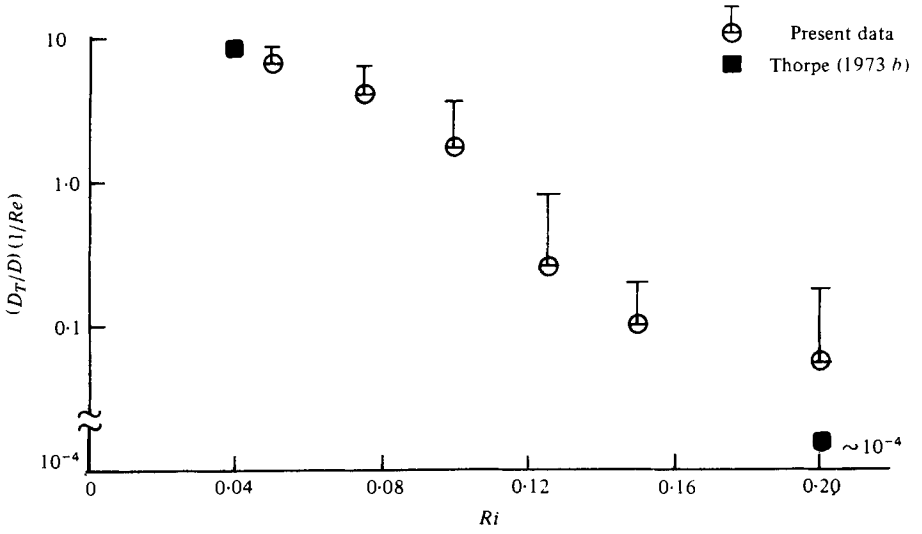

FIGURE 26. The ratio of turbulent-to-laminar diffusivity *vs.* initial Richardson numbers.

for unmixed fluid to return to its point of origin, and a consequent shortening of the time available for diffusion to take place.

Less information is available on the effect of varying Reynolds number, but the additional experiments at $Ri = 0{\cdot}075$ (figure 13) do illustrate that lower Reynolds numbers produce smaller amounts of mixing. The viscous decay of the turbulent field, as well as the buoyant redistribution of fluid, are both important in determining the amount of total mixing. The present data are not extensive enough to allow detailed conclusions about this complicated interplay, but a reasonable upper bound estimate of the total mixing can be made, as discussed in the next section.

5.4. *Extending molecular mixing results to larger Reynolds numbers*

It was suggested in the preceding sections that the turbulent event can be roughly divided into two parts: (1) the active turbulent region where only a fraction of the entrained fluid is mixed to molecular scales; and (2) the turbulent decay region where the bulk of the diffusion occurs. Can these concepts be extended to include other Reynolds numbers and other Schmidt numbers? First consider the actively turbulent portion of the flow. The interaction with the buoyancy field is of no consequence and several important results from recent experiments by Konrad (1976) and Briedenthal (1978) can be used. In a high speed mixing layer flow between dissimilar gases ($Sc = O(1)$), Konrad (1976) has observed center-line mixedness values of approximately 0·50. At a Reynolds number, $\Delta Uh/\nu$, between 10^4 and 2×10^4, a discrete transition to smaller scales occurs, and the mixedness is increased to about 0·60. Apparently, no further change in mixedness occurs with additional increase in Reynolds number. Breidenthal (1978) has observed the same transition to small scales by measuring product formation in a dilute phenolphthalein solution with $Sc = O(10^3)$. The centre-line mixedness values were negligibly small below the transition Reynolds number, and lie well below the $Sc = O(1)$ values at higher Reynolds numbers (at least to $Re = 5 \times 10^7$). It is possible to conclude that there will always

be a significant portion of unmixed fluid in the actively turbulent region, especially for larger Schmidt numbers. (For thermally stratified waters, $Sc = O(10)$, and the mixedness will still be small.)

The termination of the actively turbulent region supplies the initial condition for the subsequent downstream diffusion by bringing into close contact a certain quantity of fluid, i.e. that fluid entrained into the mixing layer at the point of maximum thickness. The quantity of mixed fluid was earlier expressed as the integral thickness, δ_f. It can also be expressed in the form of an equivalent turbulent diffusivity (Thorpe 1973*b*). The equivalent diffusivity is given by

$$D_T = \delta_f^2/16t_f = \delta_f^2\overline{U}/16x_f.$$

Thus over the period of time, t_f (or distance x_f), the mixed region grows *as if* it were diffusing at the average rate D_T. The equivalent diffusivity can be made non-dimensional with an appropriate length scale and velocity scale – say h_i and ΔU. The non-dimensional diffusivity can be expressed as a function of all other important non-dimensional variables,

$$D_T/\Delta U h_i = f(Ri, Re, Sc).$$

The ratio D_T/D is the equivalent turbulent diffusivity divided by the molecular diffusivity and is related to the Cox number found in oceanographic literature. Using the above result, this ratio is

$$D_T/D = Re\,Sc\,f(Ri, Re, Sc),$$

or, incorporating the Schmidt number dependence in some new functional,

$$D_T/D = Re\,g(Ri, Re, Sc).$$

Diffusivities for this single, isolated turbulent event are plotted in figure 26 as a function of the Richardson number. We have chosen to plot D_T/DRe to remove the obvious portion of the Reynolds number dependence. The results illustrate that, although the mixing falls off rapidly with increasing Richardson number, it does not fall to zero. An *additional* upper bound estimate on the amount of mixing can be made simply by replacing the final value of δ, δ_f, with the larger value at the point of maximum thickness, δ_{MAX}. The rationale is that at sufficiently large Reynolds numbers, or smaller Schmidt numbers, all of the fluid entrained in the turbulent growth region could ultimately become mixed in the molecular sense. These results are shown plotted as the upper bars in figure 26.

6. Concluding remarks

We have attempted to study some of the characteristics of turbulence produced in a stratified fluid for conditions which might approximate those found in the ocean. It is apparent that Richardson number, Reynolds number and Schmidt number have an important influence on the properties of the turbulence, and it is probable that oceanic mixing, occurring at Reynolds numbers of $O(10\,000$–$50\,000)$, is similarly dependent. The problem is thus complicated by the number of parameters involved including the several geometrical features which define the initial instability. We had elected the 'broad brush' approach, but were truly overwhelmed by the size of the task. Much of the parameter space at larger Richardson number and larger Reynolds number remains

to be studied, as well as the effect of varying Schmidt number. The collapse and relaminarization process deserves more careful scrutiny, and the similarity between this process and the decay of grid-produced turbulence should be explored. We were also unprepared for the complexity of the instability which appears in certain Richardson number ranges. There seem to be regions where linear, three-dimensional waves can exist. Such three-dimensional instabilities have often been ignored in the study of parallel shear flows. In this case, a profitable approach would be to combine an experimental and theoretical effort.

We gratefully acknowledge the financial support of the Office of Naval Research contract N 00014-76-C-0211 and the National Science Foundation grant ENG 73-04057.

REFERENCES

BREIDENTHAL, R. E. 1978 A chemically reacting, turbulent shear layer. Ph.D. thesis, California Institute of Technology.

BROWAND, F. K. & WANG, Y. H. 1972 An experiment on the growth of small disturbances at the interface between two streams of different densities and velocities. *Int. Sym. Stratified Flows, Novosibirsk, USSR, ASCE Publication, N.Y.* 1973.

BROWAND, F. K. & WINANT, C. D. 1973 Laboratory observations of shear-layer instability in a stratified fluid. *Bounary Layer Met.* **5**, 67.

BROWN, G. & ROSHKO, A. 1974 On density effects and large structure in turbulent mixing layers. *J. Fluid Mech.* **64**, 775.

CORCOS, G. & SHERMAN, F. 1976 Vorticity concentrations and the dynamics of unstable free shear layers. *J. Fluid Mech.* **73**, 241.

DELISI, D. & CORCOS, G. 1973 A study of internal waves in a wind tunnel. *Boundary Layer Met.* **5**, 121.

HAZEL, P. 1972 Numerical studies of the stability of inviscid stratified shear flows. *J. Fluid Mech.* **51**, 39.

HINZE, J. O. 1959 *Turbulence: An Introduction to its Mechanism and Theory.* McGraw-Hill.

HOLMBOE, J. 1962 On the behaviour of symmetric waves in stratified shear layers. *Geofys. Publ.* **24**, 67.

KONRAD, J. A. 1976 An experimental investigation of mixing in two-dimensional turbulent shear flows with applications to diffusion-limited chemical reactions. *Proj. SQUID Tech. Rep.* CIT-8-PU, *Purdue Univ. W. Lafayette, Indiana.*

KOOP, C. G. 1976 Instability and turbulence in a stratified shear layer. Ph.D. thesis, University of Southern California. (Also published as DDC Rep. ADA 026634.)

LIEPMANN, H. W. & LAUFER, J. L. 1947 Investigation of free turbulent mixing. *N.A.C.A. Tech. Note*, no. 1257.

LIN, J. T. & PAO, Y. H. 1979 Wakes in stratified fluids. *Ann. Rev. Fluid Mech.* **11**, 317.

MAXWORTHY, T. & BROWAND, F. 1975 Experiments in rotating and stratified flows: oceanographic applications. *Ann. Rev. Fluid Mech.* **7**, 273.

SCOTTI, R. S. & CORCOS, G. M. 1972 An experiment on the stability of small disturbances in a stratified shear layer. *J. Fluid Mech.* **52**, 499.

THORPE, S. A. 1973*a* Turbulence in stably stratified fluids: a review of laboratory experiments. *Boundary Layer Met.* **5**, 95.

THORPE, S. A. 1973*b* Experiment of instability and turbulence in a stratified shear flow. *J. Fluid Mech.* **61**, 731.

WEIDMAN, P. D. & BROWAND, F. K. 1975 Analysis of a simple circuit for constant temperature anemometry. *J. Phys. E: Scientific Instruments* **8**, 553.

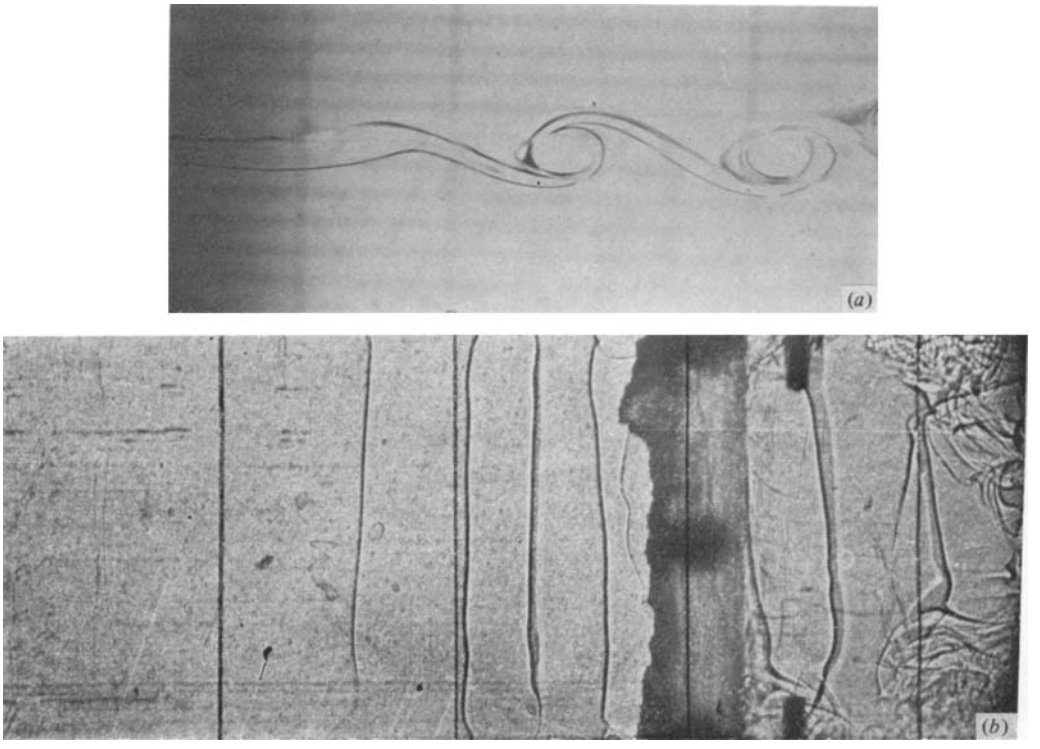

FIGURE 4. General appearance of the initial instability; $Ri = 0{\cdot}075$, $Re = 300$. (*a*) Side view with dye injected above and below the shear region. (*b*) Wave fronts viewed from above using a shadowgraph.

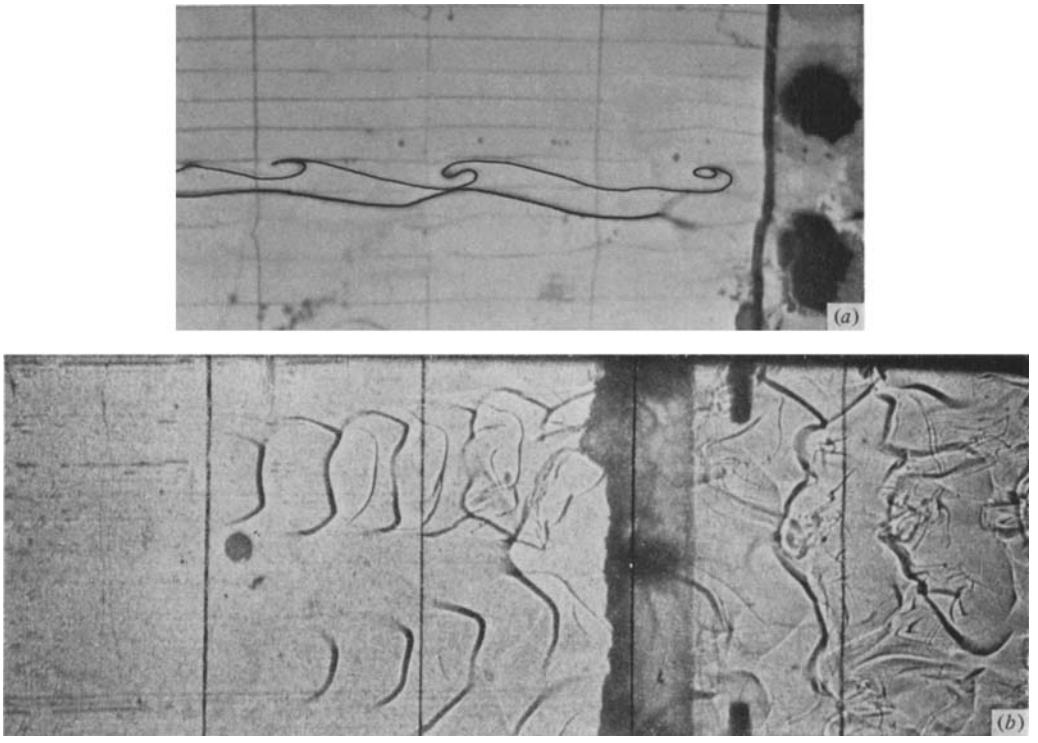

FIGURE 5. General appearance of the initial instability; $Ri = 0{\cdot}20$, $Re = 300$. (*a*) Side view, both dye lines below the shear region but separated laterally by 1 cm. (Waves have been enhanced with ink.) (*b*) Wave fronts viewed from above using a shadowgraph.

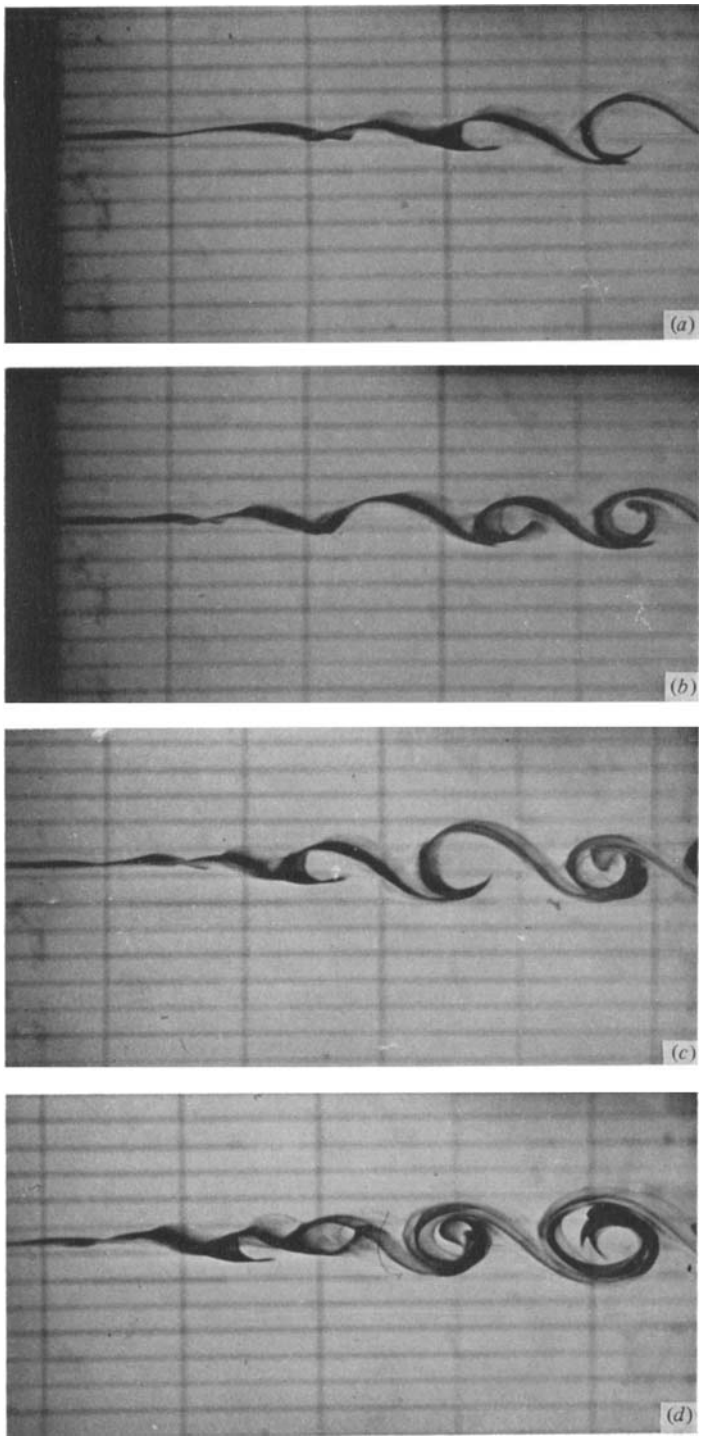

FIGURE 6

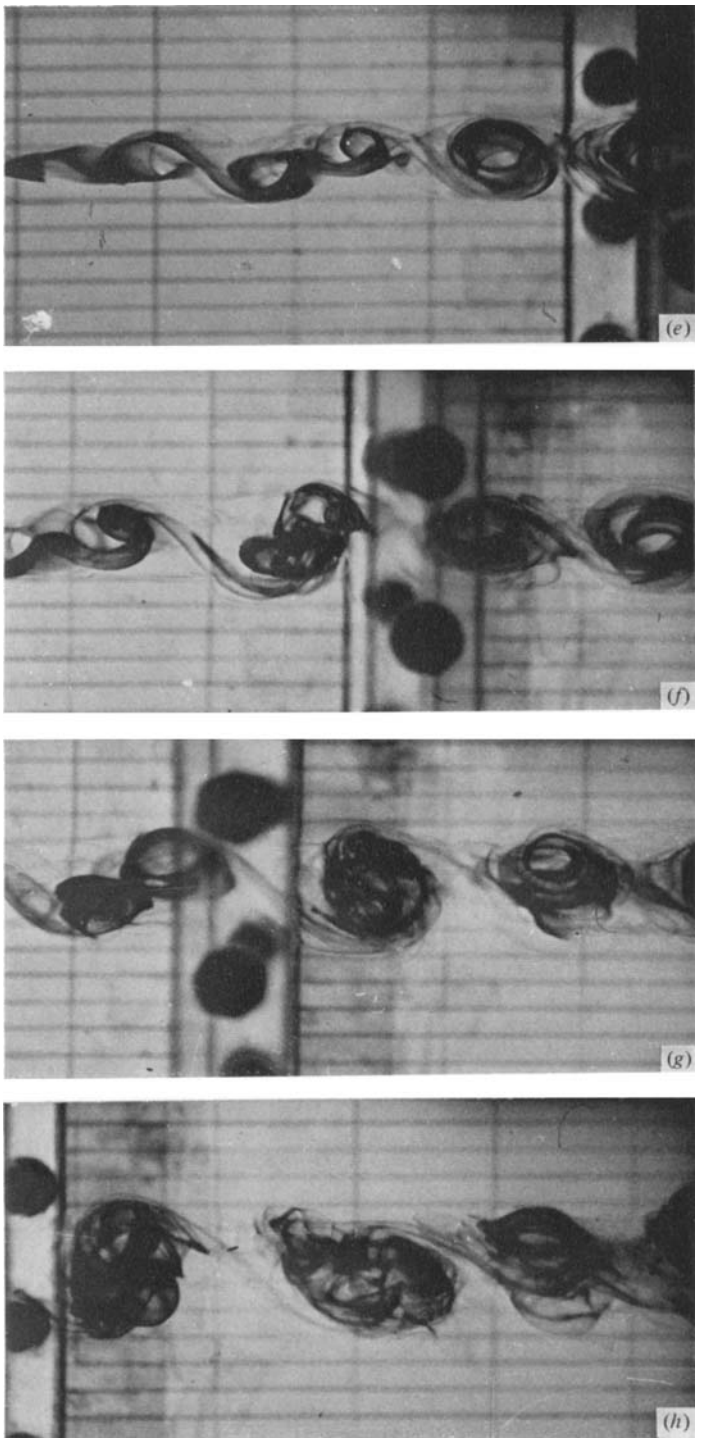

FIGURE 6

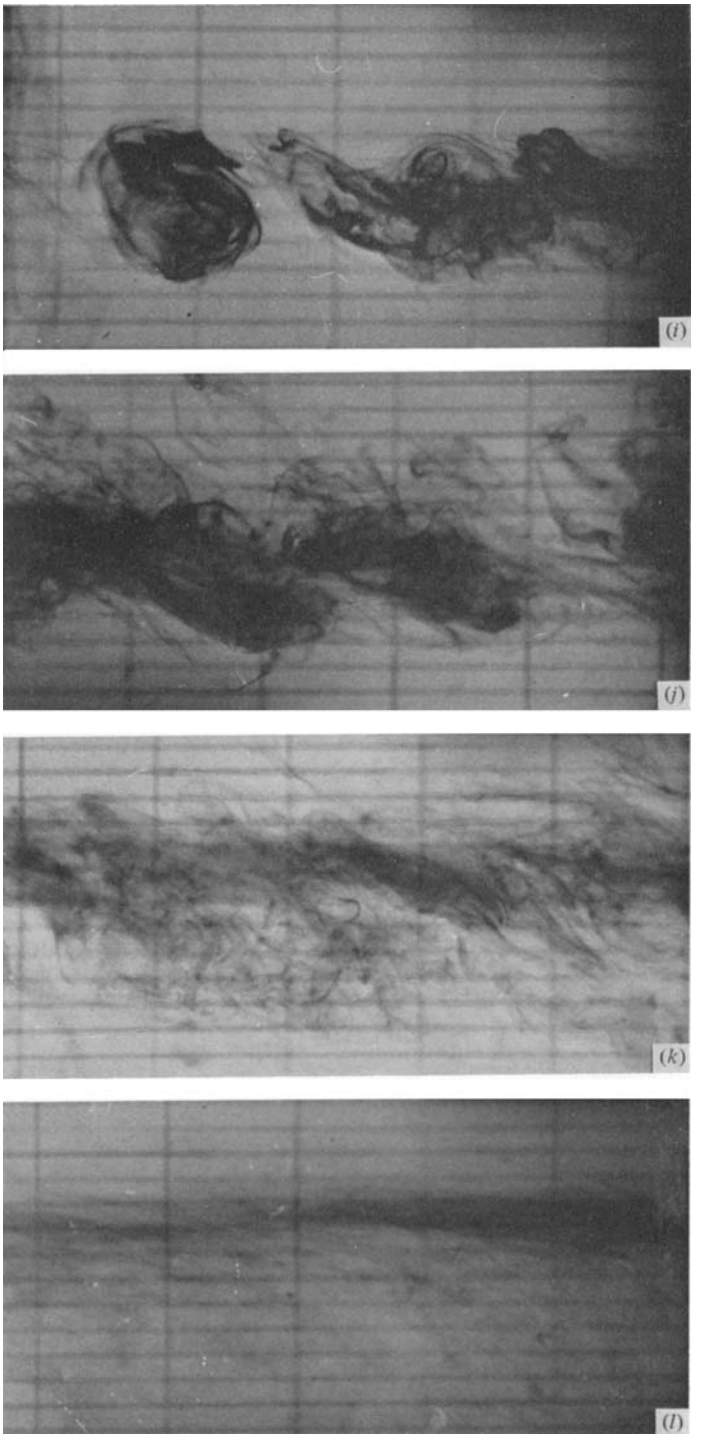

FIGURE 6. Downstream evolution of the mixing layer for $Ri = 0{\cdot}04$, $Re = 300$. Flow is visualized with dye; the camera is towed at the speed $\bar{U}$. The following x locations correspond to the longitudinal position of the picture centre in cm: (*a*, *b*) 5; (*c*) 6; (*d*) 7·5; (*e*) 10; (*f*) 12·5; (*g*) 16; (*h*) 20; (*i*) 25; (*j*) 45; (*k*) 80; (*l*) 120.

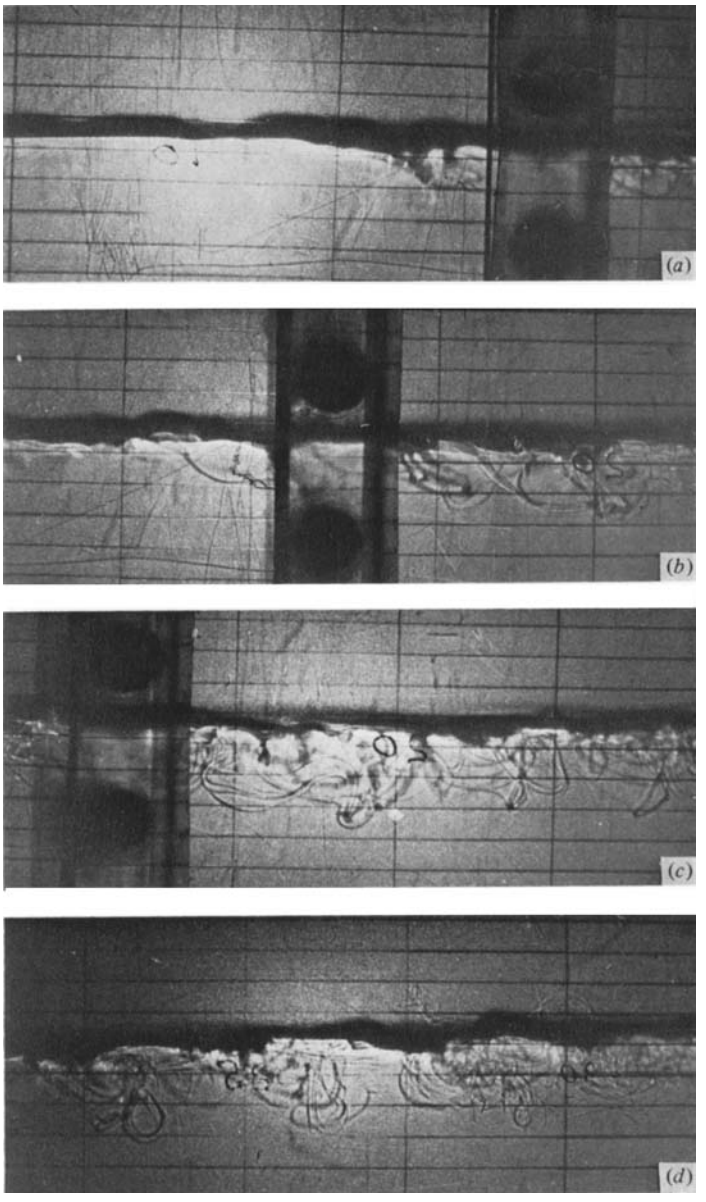

FIGURE 7

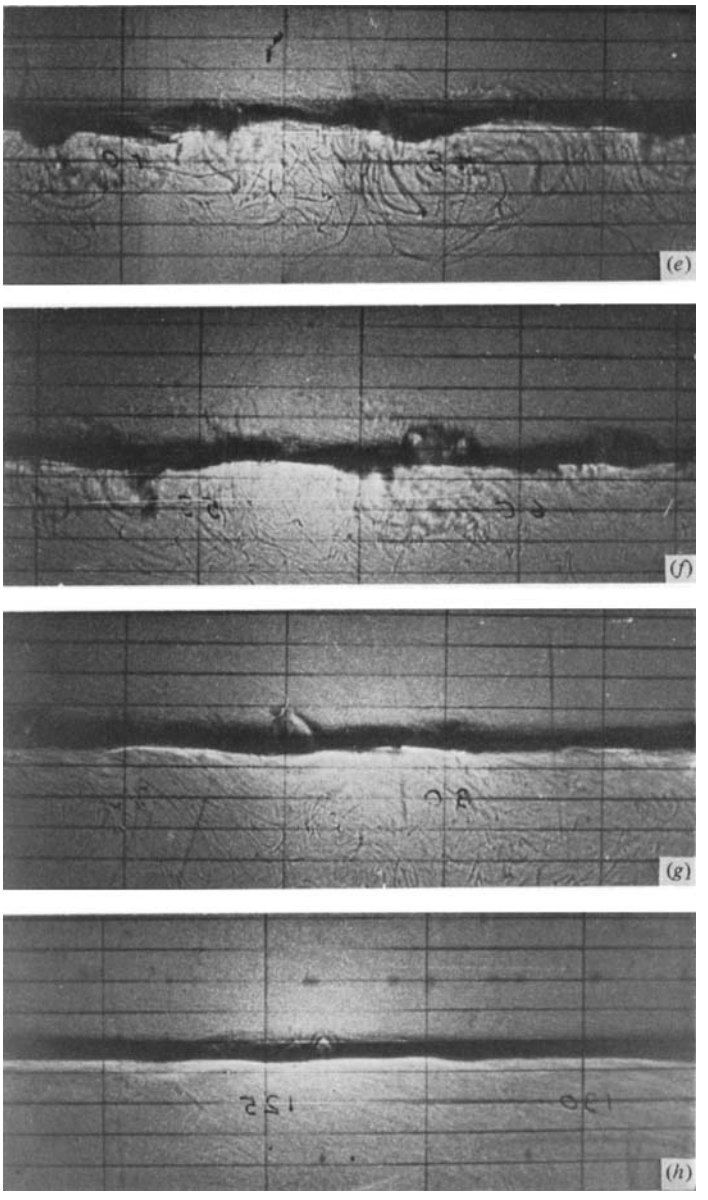

FIGURE 7. Downstream evolution of the mixing layer for $Ri = 0{\cdot}20$, $Re = 300$. Flow is visualized with a shadowgraph; the camera is towed at the speed $\bar{U}$. The following x locations correspond to the longitudinal position of the picture centre in cm: (*a*) 12·5; (*b*) 15; (*c*) 19; (*d*) 27·5; (*e*) 42·5; (*f*) 57·5; (*g*) 78; (*h*) 127.

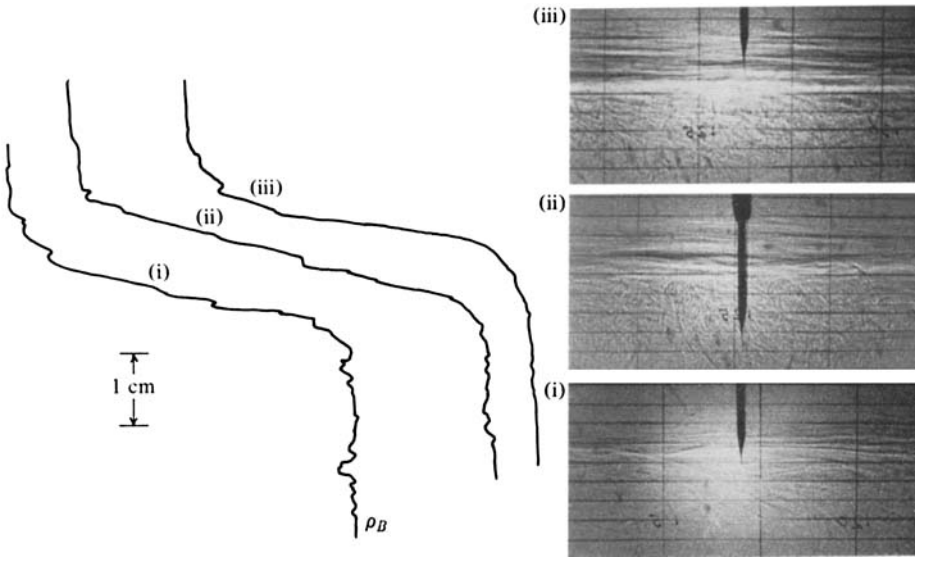

FIGURE 24. Examples of instantaneous density distribution at far downstream stations for $Ri = 0{\cdot}075$ and various Reynolds numbers. (i) $x/\theta_i = 1400$, $Re_{MAX} = 1000$; (ii) $x/\theta_i = 1200$, $Re_{MAX} = 1500$; (iii) $x/\theta_i = 1000$, $Re_{MAX} = 1750$.